A&A 386, 633–645 (2002)
DOI: 10.1051/0004-6361:20020220

Astronomy & Astrophysics

The structure and dynamics of the molecular envelope of M 2−56⋆

A. Castro−Carrizo[1], V. Bujarrabal[1], C. Sánchez Contreras[1,2], J. Alcolea[1], and R. Neri[3]

[1] Observatorio Astronómico Nacional (IGN), Apdo. 1143, 28800 Alcalá de Henares, Spain
e-mail: carrizo,bujarrabal,j.alcolea@oan.es
[2] Jet Propulsion Laboratory, MS 183-900, California Institute of Technology, Pasadena, CA 91109, USA
e-mail: sanchez@eclipse.jpl.nasa.gov
[3] IRAM, 300 rue de la Piscine, 38406 St Martin d'Hères, France
e-mail: neri@iram.fr

Received 31 October 2001/ Accepted 7 February 2002

Abstract. M 2−56 is a protoplanetary nebula (PPN) in which strong shocks are taking place, therefore, useful to study the post−AGB wind interaction. It is well known that molecular observations allow studying the mass distribution of PPNe, even in those regions that have been recently shocked. We present high−resolution maps of the emission of ^{12}CO $J=2-1$ and $J=1-0$ in M 2−56. Such maps show a bipolar, molecular nebula that extends $\sim$28″ along the symmetry axis. The nebula is composed of two contiguous, incomplete shells located along the symmetry axis, which has an inclination of $\sim$17° with respect to the plane of the sky. Those empty lobes intersect in the center of the nebula, where there is a small and dense ring perpendicular to the axis. This central ring expands radially at about 8 km s^{-1} and seems to be the remnant of the circumstellar envelope of the AGB star, that has not been accelerated by the interaction with the fast post−AGB jets. The radius of the central ring is of $\sim 4\times10^{16}$ cm, for a distance of 2.1 kpc (deduced from an analysis of the main properties of the object). At $\sim 4\times10^{17}$ cm from the nebular center, the tips of the lobes reach axial expansion velocities of $\sim$200 km s^{-1}. We have developed a model for the spatio−kinematical distribution and the excitation conditions of the molecular gas in M 2−56. From the best fitting of the observations with the predictions of the model for both lines, we have estimated the physical conditions of the molecular nebula. It is found that the density varies from 5×10^3 to 0.6×10^3 cm^{-3} from the nebular center to the lobe tips, and that the part of the lobes that has not been detected is probably composed of photodissociated gas, due to the effect of interstellar photons on low−density regions. The rotational temperature is estimated to be approximately constant, $\sim$13−16 K. For the assumed geometry, a velocity field composed by a dominant radial component plus an axial contribution has been deduced. The emission of both lines is found to be optically thin, and therefore probes the whole molecular gas, which has a mass of $\sim 0.05\,M_\odot$. The "scalar" momentum and the kinetic energy of the different regions of the molecular nebula have been calculated, finding that the high momentum won by the gas in the post−AGB phase cannot have been supplied by the radiation pressure mechanism. Although the central star of M 2−56 is not very hot yet ($\sim$20 000 K), this PPN has a large kinematical age, between 1000 yr and 1700 yr, in comparison with other PPNe that have hotter central stars. M 2−56 may not be a typical PPN, but an intermediate object between the known low−mass post−AGB nebulae and the standard PPNe.

Key words. stars: individual: M 2−56 – circumstellar matter – stars: AGB and post-AGB – radio lines: stars – stars: mass-loss

1. Introduction: M 2−56

The evolution of the stars from the asymptotic giant branch (AGB) to the planetary nebula (PN) phase is very fast, lasting a few thousand years. Few objects are therefore found in the intermediate stage, the protoplanetary nebulae (PPNe) being the surrounding envelopes of these intermediate objects. The most spectacular phenomenon that takes place in this post−AGB evolution is the ejection of very fast jets, which interact with the circumstellar envelope created along the AGB phase. This wind interaction shapes the PPNe, often becoming bipolar (Bujarrabal et al. 1998a; Sahai et al. 1998, 2000).

Send offprint requests to: A. Castro−Carrizo,
e-mail: carrizo@oan.es

⋆ Based on observations carried out with the IRAM Plateau de Bure Interferometer. IRAM is supported by INSU/CNRS (France), MPG (Germany) and IGN (Spain).

M 2−56 (IRAS 23541+7031, PK 118+08) is a PPN that has not been extensively studied up to now. The existing information mainly comes from optical and infrared data. Cohen & Kuhi (1977) classified its central star as an early Be star. HST optical observations (by Trammell & Goodrich 1998; see Fig. 3) have shown the actual bipolar structure of the source with high spatial resolution. The brightest region of both lobes is very small ($\sim 1''$), though weaker emission is found up to $\sim 5''-10''$ from the center.

Goodrich (1991) obtained optical spectra, and compared them with observed spectra of Herbig−Haro objects and with theoretical shock models, finding a good agreement for bow−shock models with shock velocities of $\sim 40-100\,\mathrm{km\ s^{-1}}$. Trammell et al. (1993) confirmed that the extended optical lines are due to local emission, and not to dust scattering, since they are unpolarized. From recent optical long−slit observations, Sánchez Contreras et al. (in preparation) have studied the dynamics of the shock−heated atomic gas, showing that it reaches velocities up to $\sim 1400\,\mathrm{km\ s^{-1}}$ in the inner part of the lobes.

A distance of $\sim 3\,\mathrm{kpc}$ was estimated by Goodrich (1991) from the assumption of a typical luminosity for standard PPNe of $\sim 10^4\,L_\odot$. For the time being we will adopt this value for our calculations, although after a wide study we will prove that the distance is probably slightly shorter, $\sim 2.1\,\mathrm{kpc}$ (see Sect. 5).

In the radio range, Bujarrabal et al. (2001) have obtained observations of M 2−56 of the transitions $J=2-1$ and $1-0$ of ^{12}CO and ^{13}CO with the 30 m radiotelescope of IRAM. Those authors studied the mass for the molecular nebula, that was found to be $\sim 0.1\,M_\odot$, and the dynamics of different spectral components: the low−velocity component probably coming from the remnant of the AGB envelope, and the high−velocity components coming from the circumstellar gas accelerated by the post−AGB wind. The linear momentum carried by the fast outflows was found to be too high to be supplied by the pressure of the stellar radiation. Note that in most PPNe most of the gas is molecular and that, in well studied PPNe, CO observations have allowed probing into the complex nebular dynamics (Bujarrabal et al. 1998b; Alcolea et al. 2001).

However, a detailed study of the dynamics and of the spatial distribution of the molecular nebula can only be performed from arcsecond−resolution maps of CO emission. In M 2−56 such a study is favored by the fact that these lines probably are optically thin (Bujarrabal et al. 2001). For this purpose we have mapped the emission of the rotational transitions CO $J=2-1$ and $J=1-0$ in M 2−56, using the Plateau de Bure Interferometer (PdBI).

2. Interferometric observations and data reduction

We have observed the emission of the rotational transitions ^{12}CO $J=2-1$ at 1.3 mm (230.538 GHz) and ^{12}CO $J=1-0$ at 2.6 mm (115.271 GHz) coming from M 2−56 (assumed J2000 central coordinates: $23^{\rm h}56^{\rm m}36\overset{\rm s}{.}38$, $+70^\circ 48' 17\overset{''}{.}9$), with the IRAM interferometer at Plateau de Bure (PdB, France). This array consists of 5 antennas of 15 m in diameter with dual−band SIS heterodyne receivers (see more details in Guilloteau et al. 1992). The observations were obtained in two different epochs. In April and May 1998 we observed the nebula, pointing just at its center, with configurations D and C1. Due to the large extent found for this source, up to $\sim 32''$ along the east−west direction, in July, August and September 1999 we carried out a mosaic with configuration D, observing 3 different points of the nebula; the center ($0''$, $0''$), and the offset positions ($-11''$, $0''$) and ($11''$, $0''$). The calibration was performed in the standard way with the GILDAS software package. The primary flux calibrator used was MWC 349. In order to mix all the observed data we followed the analysis procedure for a mosaic of 4 points. The maps were corrected for primary beam attenuation. The widths of the CLEANed beams (half−power contour) are $1\overset{''}{.}9\times 1\overset{''}{.}8$ at a PA of 115° for the CO $J=2-1$ map, and $3\overset{''}{.}9\times 3\overset{''}{.}7$ at a PA of 164° for the CO $J=1-0$ map. The conversion factors from flux units to main−beam temperature are 6.7 K per Jy beam^{-1} and 6.5 K per Jy beam^{-1} at 1.3 mm and 2.6 mm respectively. We have averaged the velocity channels of the maps of both lines to get a final velocity resolution of $3.25\,\mathrm{km\ s^{-1}}$. The final maps of CO $J=2-1$ and $J=1-0$ are shown in Figs. 1 and 2 respectively.

2.1. Flux loss estimates

In order to estimate the possible flux losses of our interferometric observations, we have compared them with the CO(2−1) and CO(1−0) profiles presented by Bujarrabal et al. (2001), obtained with the IRAM 30 m radiotelescope at Pico de Veleta (PdV). For that, several factors must be taken into account: 1) the detection of the emission found at more than $\sim 12''$, from the center, becomes very difficult from the PdV observations by Bujarrabal et al., even with the largest beam. 2) The velocity resolutions of both observations, of PdB and PdV, are different.

In a first procedure to estimate a possible flux loss, we have CLEANed our dirty maps convolving the CLEAN components with the PdV beam. Then the main−beam temperatures obtained have been compared with the PdV profiles, also given in $T_{\rm mb}$ units. In a second procedure, we have used the model calculations that fit our data (see Sect. 3.2). We have convolved the brightness distribution predicted by that model with the PdV beam, and so we have obtained the PdV $T_{\rm mb}$ for each velocity channel. In both cases very similar results have been obtained: for the CO(2−1) line the flux obtained in PdB is ∼30% lower than that observed in PdV, and for the CO(1−0) line the flux obtained in PdB is ∼10% lower than that from PdV. Since this flux difference of ∼30% is approximately constant for all the velocities of the CO(2−1) profile, we suspect that it may be a consequence of a wrong absolute flux calibration, instead of a flux loss in the interferometric observations.

Note anyway that a calibration uncertainty of ∼30% is moderate, and that is within the typical uncertainties. In

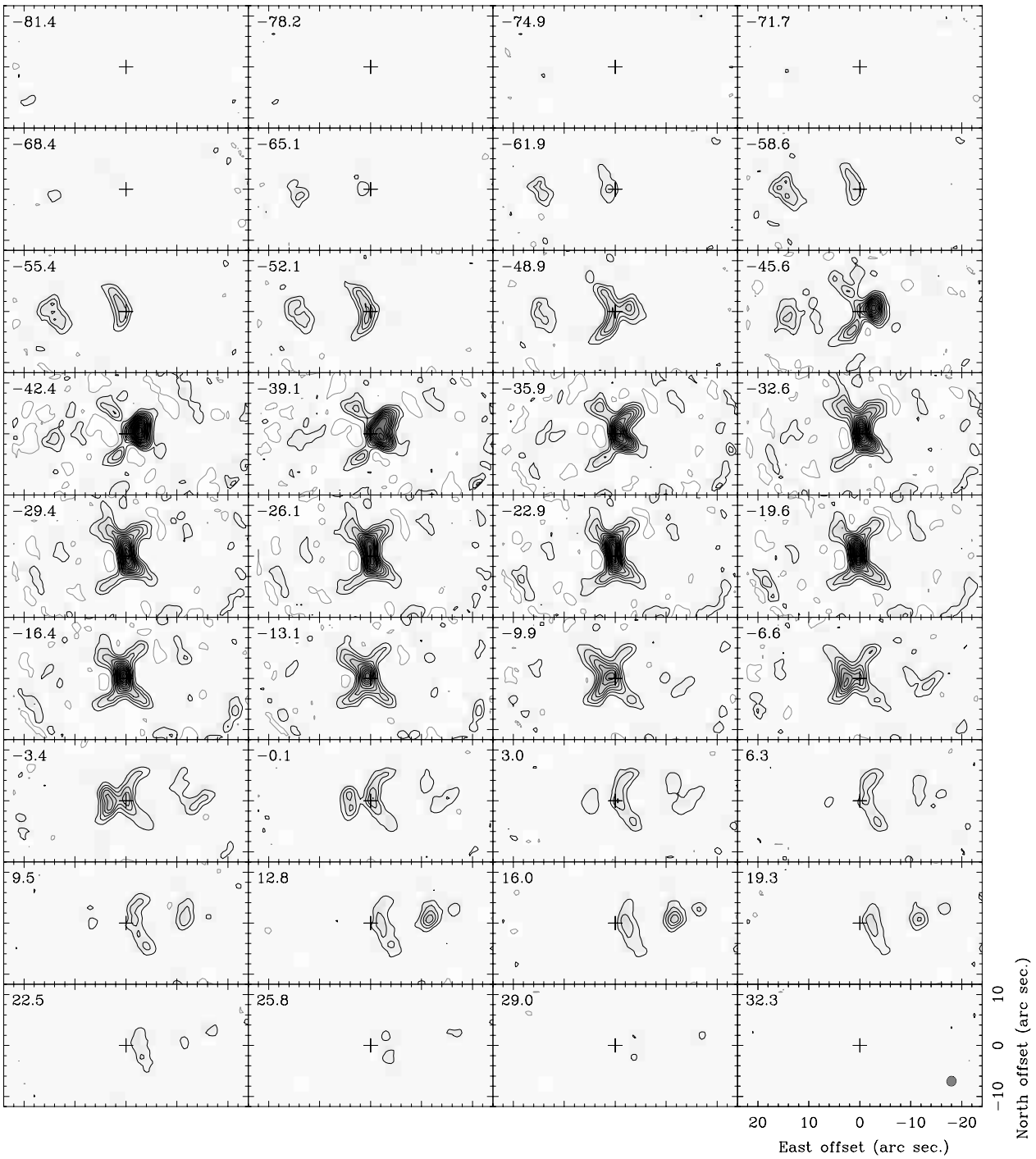

Fig. 1. PdBI maps of CO $J=2-1$ emission from M 2−56 (J2000 central coordinates: $23^{\rm h}56^{\rm m}36\overset{\rm s}{.}38$, $+70^{\rm o}48'17\overset{''}{.}9$), for the LSR velocities indicated in the left−upper corners. The level step and the first contour, in main−beam temperature units, are 0.27 K (40 mJy/beam). The first negative level is shown in grey contour. The CLEANed beam (half−power contour) is drawn in the right−bottom corner of the last panel.

the case of a flux loss of ∼30%, the lost component must be very extended, and therefore its brightness must be very low and its effects on the total brightness distribution must also be very small. This result is moreover supported by the fact that the spatial distribution of the total CO $J=1-0$ emission is similar to that of CO $J=2-1$, and for the CO $J=1-0$ maps a significant flux loss is not expected. So, we have not introduced any correction in our maps (Figs. 1 and 2) due to this effect (possible flux loss or uncertainty in the flux calibration), though it will be taken into account when they are compared with our model predictions (Fig. 4).

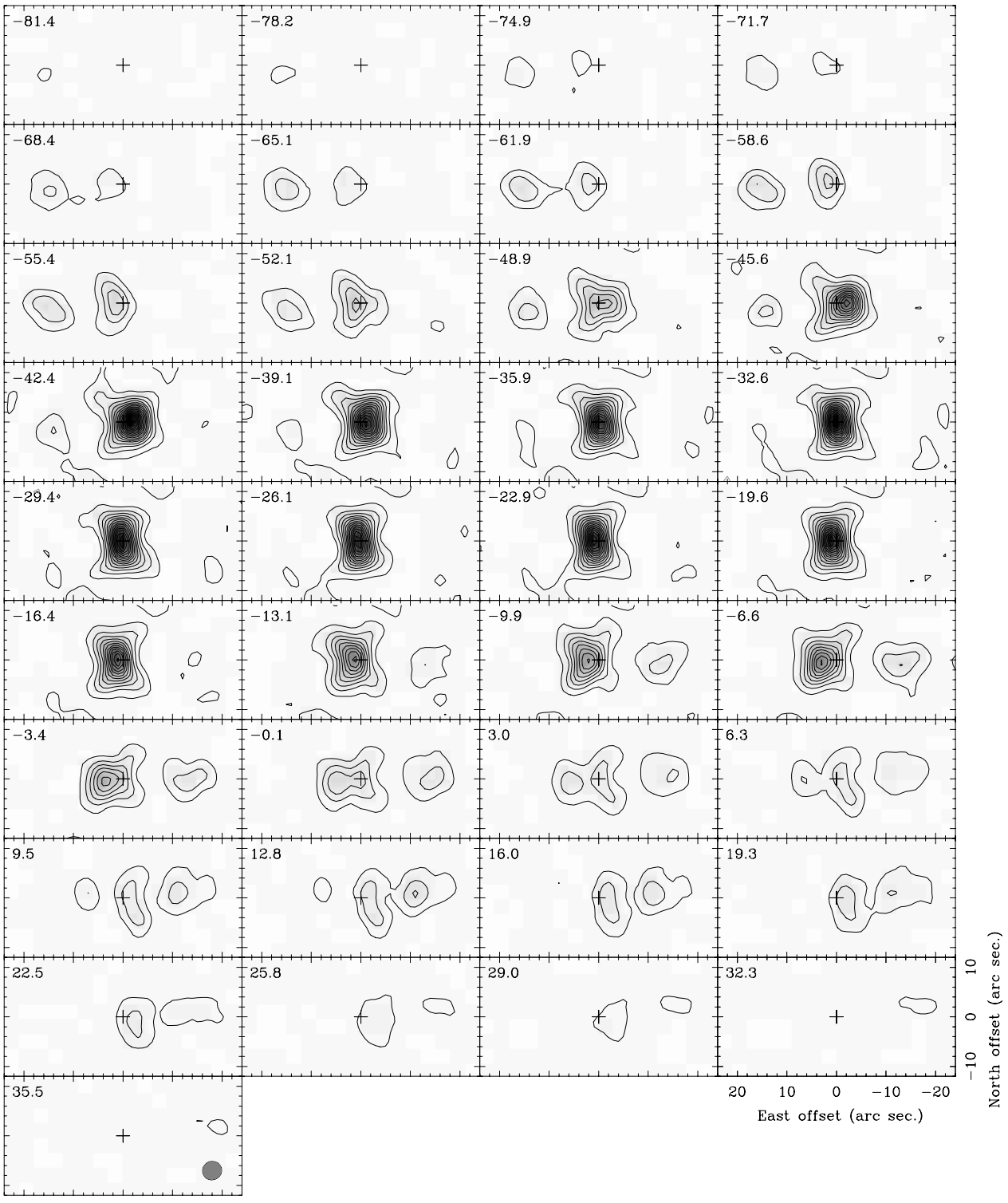

Fig. 2. PdBI maps of CO $J = 1-0$ emission from M 2−56, for the LSR velocities indicated in the left−upper corners. The level step, in main−beam temperature units, is 0.13 K (20 mJy/beam) being the first level at 0.065 K (10 mJy/beam). No negative levels at −0.065 K are present. The CLEANed beam (half−power contour) is drawn in the right−bottom corner of the last panel.

3. Analysis of the CO mapping

3.1. Maps of the CO(2−1) and CO(1−0) emission

In Fig. 1 we present the CLEANed maps of the CO $J = 2-1$ line emission, and in Fig. 2 those of CO $J = 1-0$. In this section we deduce directly from the observations some parameters on the nebular gas distribution, which will be used as input data in the nebular model described in Sect. 3.2.

A first inspection of the maps suggests that the nebula is axially symmetric, the axis being very close to the east−west direction. We find an X−shaped structure in the central part of the nebula, that is expanding at low velocity, and two high−velocity clumps at 11−15″ from the center along the symmetry axis. This structure, that resembles that seen in other PPNe (see, for instance, Bujarrabal et al. 1998b), allows inferring the gas distribution. The CO emission is probably coming from a bipolar nebula composed of two incomplete and contiguous shells that join in the center of the nebula, where an intense emission feature is observed perpendicular to the symmetry axis. These lobes would be expanding along this axis, which seems to be almost perpendicular to our line of sight. The described structure agrees well with the idea that such a bipolar nebula is the result of the interaction between fast and collimated post−AGB winds and the circumstellar envelope ejected in the AGB phase. So, the slowly expanding, compact central emission elongated perpendicularly to the nebula axis is probably the remnant of the AGB circumstellar envelope that has not been accelerated by the fast axial jets, shaping a ring or disk−like region (which seems to be almost edge−on) perpendicular to the symmetry axis.

Note the lack of detection of CO emission in an extended part of the shells, from 6″ to 11″ from the nebular center. Such an absence of emission could be related to the dilution of the gas due to expansion, to the photodissociation of the CO molecules, or to a change of the excitation conditions. In Sect. 5.1 we analyze those possibilities, and we conclude that the shells are probably complete, comparable to those of M 1−92 (Bujarrabal et al. 1998b), the gas in the undetected regions being photodissociated.

We have assumed a systemic velocity of $-26.1\,\mathrm{km\ s^{-1}}$ LSR, though the gas distribution is not exactly symmetrical with respect to this channel (see Fig. 1). We will analyze those asymmetries in Sect. 3.2. The maximum expansion velocity (projected on the line of sight) found from CO(2−1) is about $50\,\mathrm{km\ s^{-1}}$, and from CO(1−0) about $60\,\mathrm{km\ s^{-1}}$. This noticeable difference could be due to the flux loss of the CO(2−1) observations, as well as to a gradual change of the excitation conditions along the axis, for example to a slight outwards decrease of the gas temperature. For the CO(2−1) maps, the main−beam temperature (T_{mb}) in the nebular center at the systemic velocity is ∼3.2 K, but the peak temperature (∼4.5 K) is found for the velocity panel at $\sim -42.4\,\mathrm{km\ s^{-1}}$, whose high intensity has been interpreted as a result of one of the above mentioned asymmetries. For the CO(1−0) line, the T_{mb} in the center at the systemic velocity is ∼1.7 K, and the peak temperature (∼2.1 K) has been found for the same velocity channel as for CO(2−1).

In the central panels of the CO(2−1) maps, in which the peak intensity is higher, the sensitivity is limited by a maximum dynamical range of ∼13 due to uncertainties in the amplitude and phase calibration. This yields spurious features that are responsible for the extra noise seen in the position−velocity diagrams *a* and *b*, at $\sim -40\,\mathrm{km\ s^{-1}}$ (Fig. 3). Such features are not present in the CO(1−0) maps.

Let us analyze now the dimensions of the nebula, from our CO(2−1) maps. For the distance assumed from Goodrich (1991), 3 kpc, we obtain that the extent of the nebula in its axial direction, projected in the sky plane, is $\sim 1.2 \times 10^{18}$ cm. That value is comparable with the typical size found in other PPNe, so we conclude that the assumed distance cannot be wrong by a large factor. The very intense, central region elongated perpendicularly to the axis extends about 4×10^{17} cm in this direction, and $\sim 1.3 \times 10^{17}$ cm in the axial direction. The position angle (PA, measured from North to East on the plane of the sky) of the symmetry axis has been measured to be 94° from our observations.

In order to study in depth the emission coming from different regions, we have shown four position−velocity diagrams along representative axes (see Fig. 3). From diagrams *a* and *b* we analyze the emission from the center, which, as mentioned before, seems to come from a ring. This distribution is confirmed by the double peak seen in diagram *a* and by the central ring−shaped emission in diagram *b*. Note that diagram *b* shows the emission from (almost) the whole ring, since it seems approximately edge−on, whereas diagram *a* shows the emission from the central part of the ring. If we assume that the typical ring radius is defined by the intensity peak in both diagrams, and we compare the size of the ring obtained from both cuts, which are related through the sine of the inclination of the axis with the sky plane, then we obtain that such an inclination is $\sim 17^{\circ} \pm 2^{\circ}$, confirming that the ring is approximately edge−on, and that the typical ring radius is $\sim 6 \times 10^{16}$ cm. From the velocity of the components of each lobe we find that the east−lobe is the closest to us. The ring is found to expand radially at ∼7–8 $\mathrm{km\ s^{-1}}$, from both position−velocity diagrams.

From diagrams *c* and *d*, Fig. 3, we analyze the emission coming from two axes perpendicular to the nebula axis and displaced 2.″64 from the center. They allow studying the intensity peak found at about $-44\,\mathrm{km\ s^{-1}}$, and the spatially symmetrical (but weaker) emission found at about $-5\,\mathrm{km\ s^{-1}}$. One would expect to find similar relative maxima in diagrams *c* and *d* as a consequence of a projection effect, however, the maximum in plot *d* is much stronger than that seen in *c*, and even stronger than that found at the nebular center. The predictions of the models (discussed in Sect. 3.2) cannot reproduce this so intense maximum at $\sim -44\,\mathrm{km\ s^{-1}}$, but just a relative maximum comparable to that seen at $\sim -5\,\mathrm{km\ s^{-1}}$. Finally, note that this maximum at $\sim -44\,\mathrm{km\ s^{-1}}$ is not directly related to the central ring. We suggest that the maximum at $\sim -44\,\mathrm{km\ s^{-1}}$ is just the result of a very dense clump in the west−lobe wall closest to us. As we have mentioned, due to this high intensity, some spurious features have been found for those velocity channels (from $-40\,\mathrm{km\ s^{-1}}$ to $-46\,\mathrm{km\ s^{-1}}$), becoming quite remarkable in diagram *b*, Fig. 3.

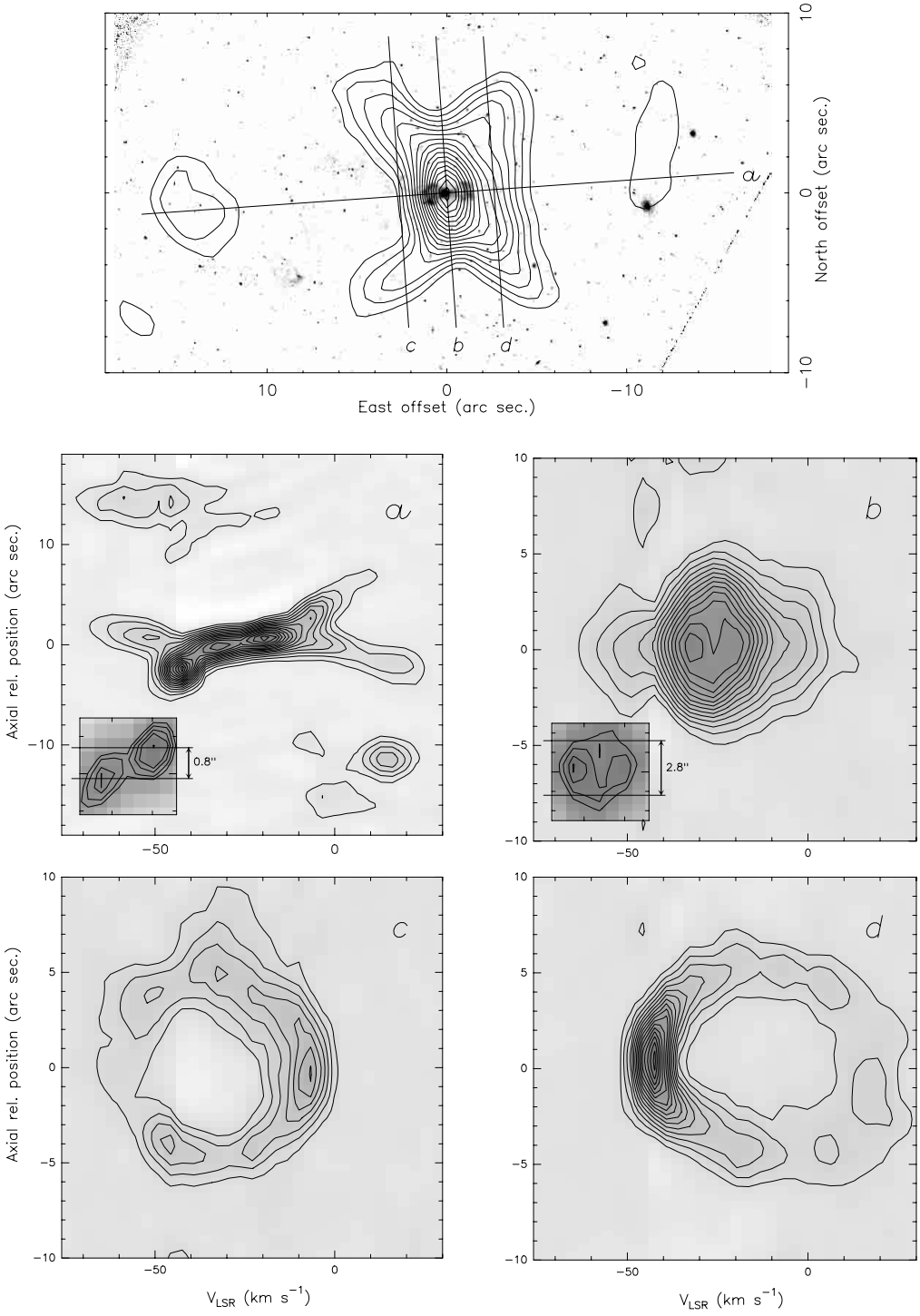

Fig. 3. The first plot shows the averaged CO(2−1) emission from M 2−56 (in contours) and the Hα+continuum HST image (in grey scale; Trammell & Goodrich 1998). The following plots show position−velocity diagrams of the CO(2−1) emission found along the axes ***a***−***d***); the level step and the first contour, in $T_{\rm mb}$ units, are 0.27 K (40 mJy/beam). Insets show expanded views of the center of ***a***) and ***b***) diagrams, with appropriate contours to estimate the size of the ring projected along each axis (the ring being always defined by maxima at the corresponding velocities).

Taking into account the inclination of the nebula axis with the sky plane, that we have found to be of $\sim$17°, we can estimate the expansion velocities of the different regions. As we have mentioned, the gas in the ring expands radially at a velocity of about 7–8 km s^{-1}. The gas in the tips of the lobes, that has been accelerated axially, must be corrected by a factor $1/\sin(17^{\rm o})$, and so we obtain a maximum expansion velocity of $\sim$170 km s^{-1} from the CO(2−1) emission, and of $\sim$210 km s^{-1} from CO(1−0). Note that, due to the uncertainty in i, there is an error bar of about $\pm$10% for the axial velocities and for the corresponding momenta. That error in the momentum is

however significantly smaller than the uncertainties due to the mass measurement (see Sects. 2.1 and 4.2). The gas of the west−lobe, that is mainly moving away from us, reaches slightly higher velocities than those found in the east−lobe. The lobe tips are in fact composed of different clumps, that are better perceived in the west−lobe. Note also that the east−lobe extends (up to 7.2×10^{17} cm, for a distance of 3 kpc) farther than the west−lobe (up to 5.8×10^{17} cm).

In the first plot of Fig. 3 we see the velocity averaged emission of the CO $J = 2-1$ line (in contours) and, by comparison, the optical HST image (in grey scale; discussed by Trammell & Goodrich 1998). Trammell et al. (1993) proved that the extended Hα emission does not come from dust scattering and confirmed the absence of a photoionized H II region. Hα emission would be then mainly tracing shocked regions, flowing at velocities as high as $\sim$1400 km s^{-1} close to the star (Sánchez Contreras et al., in preparation). Therefore, we see atomic hot gas located inside the molecular lobes, such an extended atomic emission being very intense near the star, where the shock excitation is higher.

3.2. Comparison with the emission predicted by models; estimate of the physical parameters

We have developed a code similar to that by Bujarrabal et al. (1997, 1998b) in order to model the spatio−kinematical distribution of the nebula and its excitation conditions. The model predictions for the emission of both lines, CO $J = 2-1$ and $J = 1-0$, have been compared with our data. Our code takes into account opacity effects and the radiative interaction of different parts with similar velocities projected on the line of sight. The calculated intensities are convolved with the CLEANed beams of the observations. The excitation of the two lines is assumed to be described by a single rotational temperature. As we will see, densities of $\sim 3.5-0.4 \times 10^3$ cm^{-3} have been obtained for M 2−56 (for an assumed distance of 3 kpc). So, according to the calculations shown by Bujarrabal et al. (1997), we cannot assume thermalization in the whole nebula, except for the innermost nebular regions, where maximal densities are expected.

In Fig. 4 we present the predictions of the CO(2−1) emission obtained from a nebular model such that the predicted emission for both CO(2−1) and CO(1−0) lines fits satisfactorily well the observations. In the fitting of the maps of CO(2−1) emission we have taken into account the estimated flux loss of $\sim$30% (as discussed in Sect. 2.1, see Fig. 4). The same scales and CLEANed beams have been used in both maps of observations and predictions of the emission of each line. The spatio−dynamical model of the nebula whose emission best fits the observations is shown in Fig. 5.

We have assumed that the fitting between the observations and the predictions for both lines is satisfactory when 1) the differences between them for the X−shaped central part of the nebula are smaller than one contour, that is, the fitting is approximately better than 0.27 K ($\sim$8% of the peak intensity), and 2) the model predicts the mean intensity and size of the lobe−tips, in such a way that the total intensity coming from the tips coincides with that predicted with an error <8%. Note that these maximum allowed discrepancies (one contour) are given by the observational uncertainties. Following these two criteria we have determined uncertainty bars for the main parameters of the model, which are given below. Since the nebula shows some asymmetries with respect to the central velocity, point 1) is in some velocity channels not absolutely fulfilled. So, we have checked that the difference between the total intensity measured from the predicted maps and that from the observations is smaller than $\sim$10% of the total intensity, for each velocity and for each one of the three regions we distinguish in the nebula (see Sect. 4.2).

A CO abundance of 2×10^{-4} (respect to that of H_2) has been assumed; that is characteristic of PPNe with strong CO emission, where photodissociation is not very important yet (see, for example, Bujarrabal et al. 1997, 1998b; Alcolea et al. 2001). If this abundance is an overestimate, then the model densities (and so the masses, momenta and energies) would be underestimates.

We have assumed that the geometry of the nebula is axially symmetric. In the previous section the inclination of the symmetry axis with respect to the sky plane was estimated to be 17°. The central part of the nebula is supposed to be formed of two shell caps that join at the center of the nebula, as shown in Fig. 5. The lobe tips are assumed to be compact regions, that are radially more extended than the thickness of the central caps. Those shell caps intersect at the nebular center, shaping an equatorial ring. As we can directly see from the observations, there is no detection of a part of both shells, from 6 to 11″ from the nebular center. We suppose that the amount of molecular gas in those regions of our nebula (that would complete the shells from the central part to the lobe tips) is negligible.

We have obtained that the rotational temperature of the gas must be in a range of 13 to 16 K to fit the emission of both lines for most of the nebula, being therefore approximately constant (the temperature in the dense central ring probably coinciding with the kinetic temperature). In the tips of the lobes the rotational temperature becomes less constricted, between 10 K and 16 K. (Note that the observed tips show much more structure than what we have supposed, so the fitting here is less satisfactory and the constraints to the model parameters are poorer.) The predictions we show in Fig. 4 have been obtained assuming a constant rotational temperature of $\sim$14 K in the whole nebula.

In the model whose predictions best fit the data, the density decreases with the distance to the equatorial plane. We have distinguished three (density) regions; the region closer than 6.5×10^{16} cm to the equatorial plane, where the density decreases linearly from 3.5×10^3 cm^{-3} to

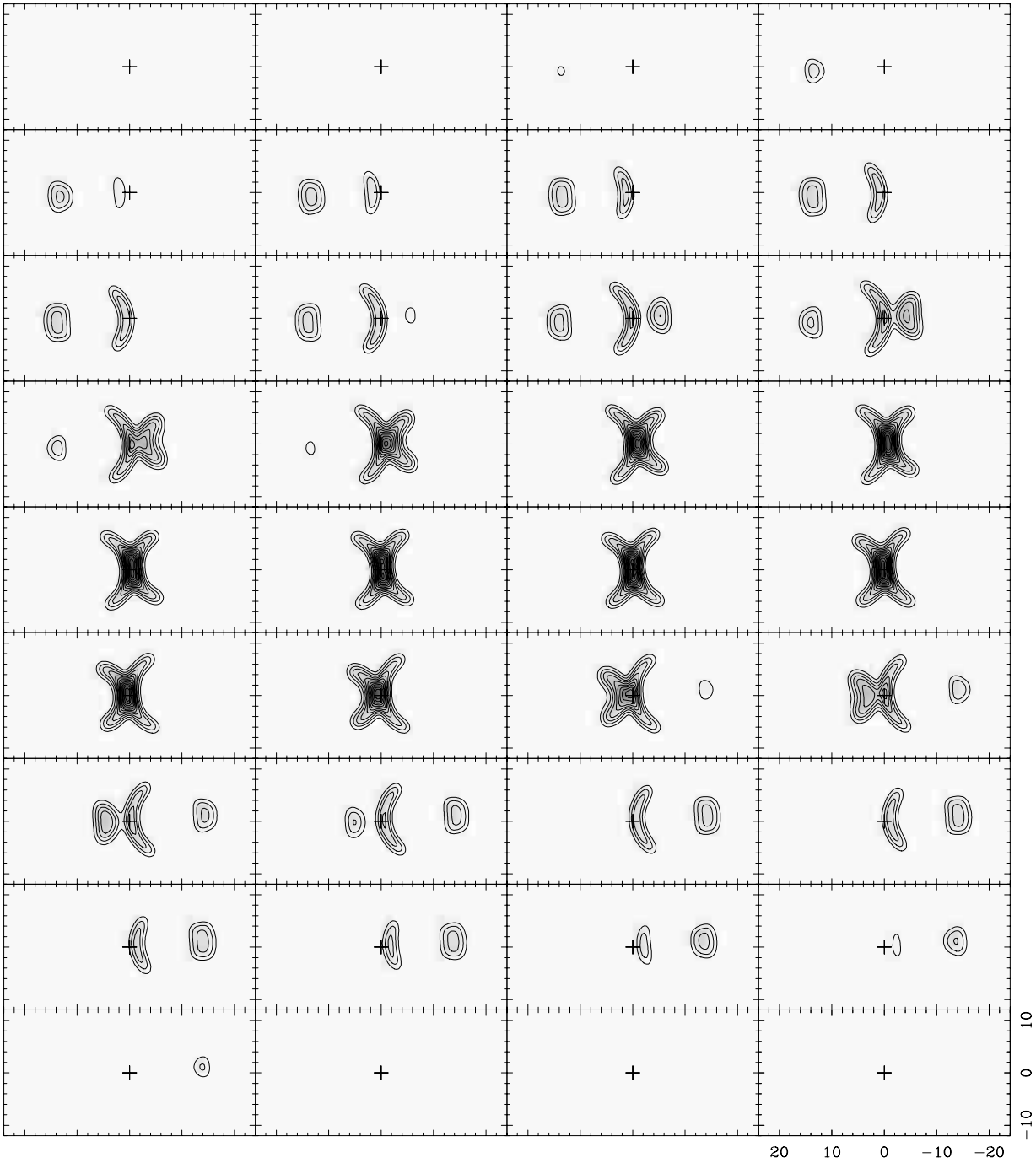

Fig. 4. Results of the model fitting to our ^{12}CO(2−1) maps of M 2−56. The velocities, spatial offsets, and the CLEANed beam are the same as in Fig. 1. The level step (0.27 K×1.3 in $T_{\rm mb}$ units) has been chosen to directly compare these predictions with the observations (shown in Fig. 1), once the flux−loss correction has been included (see Sect. 2.1).

$0.8\times10^3\,{\rm cm}^{-3}$; the region farther than 6.5×10^{16} cm, where the density goes down less sharply from $0.8\times10^3\,{\rm cm}^{-3}$ to $0.4\times10^3\,{\rm cm}^{-3}$; and the outer clumps where we have assumed a constant value of $0.4\times10^3\,{\rm cm}^{-3}$ (all figures for a distance of 3 kpc; the density distribution is shown in grey scale in Fig. 5). A change in the density of the central region higher than $0.2\times10^3\,{\rm cm}^{-3}$ would make the fitting with the observations quite unsatisfactory. The density of the undetected regions must be $<0.15\times10^3\,{\rm cm}^{-3}$ for the assumed CO abundance. This increase of the density in the nebula tips (with respect to the non−detected regions) has been also found in other PPNe, as Frosty Leo, M 1−92 and OH 231.8+4.2. At the center of the nebula, along the axis, an empty cylinder has been assumed just to fit the small relative minimum that seems to be in the center of our maps (see Figs. 5 and 3).

Our assumptions on the nebular geometry play an important role on the derivation of the velocity field, since different geometrical suppositions would lead to different velocity fields to fit the data. Taking into account

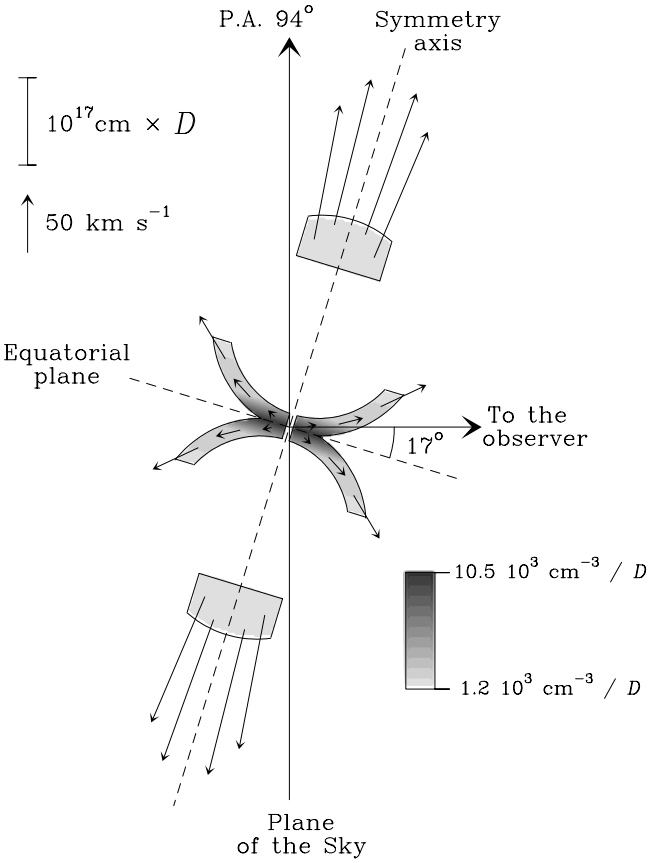

Fig. 5. Model of the emitting nebula whose emission best fits our maps of the CO(2−1) and CO(1−0) emission. The velocity field is represented by the arrows. The spatial and density scales are given as functions of the distance (D), in kpc.

the results directly derived from our maps (Sect. 3.1), we have deduced a morphology for our nebula able to fit the cross−like central feature and the outer knots. For this geometry, the velocity field that best fits our observations is composed by a radial component, that increases linearly with the radius, and an axial component, that increases linearly with the distance to the equatorial plane. In order to fit the cross−like central feature of the nebula, the radial component must be very important, reaching 85 km s^{-1} in the outer parts, where the axial component reaches a value of 40 km s^{-1}. Small changes in those values would make the fitting unsatisfactory, for the above assumptions. In Fig. 5 the assumed velocity field is represented by some velocity vectors. Although the spatial and kinematical distribution of the lobe tips is more complex than that assumed by the model, our model allows reproducing the mean intensity and extent of the tips, and therefore also their integrated intensity (i.e. their mass). Note that, probably, we could have found a velocity field exclusively radial to fit the data of the whole nebula, from our geometrical assumptions, but, in that case, the dependence on the radius would be more complex than linear.

The main difference between the model predictions and the observations is the presence of a very intense emission found in the channels from −40 km s^{-1} to −46 km s^{-1}, that our simple model cannot reproduce. Although the model predicts a relative maximum at those velocities, it is much less intense than the observed peak. This emission cannot be due to the central ring, because it is too displaced from the center. If a disk−like region or a ring was responsible for that emission at −44 km s^{-1}, an intense emission much more displaced from the center (in the perpendicular direction) than that observed would have been seen at the central channels. Such an intense feature may be due to a very dense and compact clump located in the part of the west−lobe wall that is approaching us. Note that, no counterpart of this very intense maximum has been observed at ∼−5 km s^{-1}.

The opacities obtained in the nebular center at the systemic velocity from the model, whose predictions best fit the data, are 0.86 and 0.38 for CO(2−1) and CO(1−0) respectively, indicating that, as it was proposed by Bujarrabal et al. (2001), the emission is optically thin. Only the CO(2−1) emission from the very center of the nebula approximates an optically thick case. As those authors, we have obtained a small mass for the molecular envelope of M 2−56, in comparison with other typical PPNe. Our value, 0.086 $M_\odot$, is slightly lower (Bujarrabal et al. obtained 0.1 $M_\odot$), but note that our model does not reproduce the dense clump found at about −44 km s^{-1}.

4. The kinematical post−AGB lifetimes and the dynamics of M 2−56

4.1. Kinematical post−AGB lifetimes

Two kinematical post−AGB lifetimes have been estimated from our data: 1) the time elapsed since the copious mass loss, characteristic of the ending AGB phase, ceased, and 2) the time since the wind interaction, characteristic of the PPNe, took place. For the first estimate, we have studied the emission coming from the ring, which has probably not been altered by the post−AGB ejections. Since the central ring has a typical radius of ∼6 × 10^{16} cm, and expands at about 8 km s^{-1}, we obtain a kinematical time of ∼2400 yr. Note however that the time since the mass loss process ceased is given by the minimum radius of the ring, which cannot be determined accurately for our data. So, we can only approximately say that our object left the AGB less than 2400 yr ago. On the other hand, from the tips of the lobes, which expand at ∼200 km s^{-1}, we obtain a kinematical time for the wind interaction of about 1400 yr, assuming that the wind interaction was brief and that since then the gas expands freely (as suggested for several other PPNe). The post−AGB lifetime must be, therefore, between 1400 yr and 2400 yr. Hereafter we will assume a value of ∼2000 yr.

Table 1. Main distance−dependent nebular paramenters, for both distances 3 kpc and 2.1 kpc. A distance of ∼3 kpc was obtained from a typical PPN luminosity of $10^4\,L_\odot$. In Sect. 5 we discuss that the distance of M 2−56 probably is ∼2.1 kpc, the value 2.1 kpc being the kinematic distance. Parameters are estimated in Sects. 3 and 4.

Assumed Distance:	2.1 kpc	3 kpc
Total Extent (cm)	10^{18}	1.6×10^{18}
Ring Radius (cm)	4.2×10^{16}	6×10^{16}
Density (cm^{-3})	5×10^3 to 0.6×10^3	3.5×10^3 to 0.4×10^3
Luminosity ($L_\odot$)	5×10^3	10^4
M ($M_\odot$)	0.05	0.1
P (gr cm s^{-1})	4×10^{38}	8×10^{38}
E (erg)	1.4×10^{45}	2.8×10^{45}
Post−AGB Time (yr)	1000−1700	1400−2400
Galactic Altitude (pc)	300	440

4.2. The dynamics of the different nebular components

We have determined the mass (M), the "scalar momentum" (P) and the kinetic energy (E) of the different nebular components, from our PdB data. Note that we are calculating a "scalar" momentum, that is, the addition of all the momentum moduli of each region. The nebula has been divided in three parts: the central ring, the central nebula discarding the ring, and the tips of the lobes.

The best estimate of the total mass must be obtained directly from integrating the emission detected in our maps, and then using the formulae discussed by Bujarrabal et al. (2001). Those formulae relate the molecular mass of a region (of the projected nebula on the sky plane) and the whole emission of an optically thin CO line coming from it. However, to properly derive the mass of the different regions of the nebula (some of which are not directly distinguished in the maps) we have to use our model by integrating the densities (ρ) in the selected regions. We have previously seen that the emission predicted by the model does not fit satisfactorily the observations just for the intense clump seen at ∼−44 km s^{-1}. We have estimated that an additional mass of $\sim 0.006\,M_\odot$ must be included at ∼3″ from the center in the west−lobe, to properly reproduce the observations.

In order to estimate P and E we need more information on the velocity field than that given directly from the observations. Note that we observe just the velocity projected on the line of sight, but not the velocity modulus. The velocity field is given by the nebular model whose predictions for the emission best fit our observations. P and E are obtained by integrating $\rho \times v$ and $\rho \times v^2/2$, respectively, in each region of the nebular model, where ρ is the density and v the velocity of each point of the nebula. Note that the contribution of the fast tips to the total P and E becomes very important, in spite of their small mass. Let us now estimate the contribution of the clump seen at ∼−44 km s^{-1} on the P and E estimated by the model. Since the velocity modulus of this component is probably ∼−50 km s^{-1} (see Fig. 5) and its mass is $\sim 0.006\,M_\odot$, its momentum becomes $\sim 6 \times 10^{37}$ gr cm s^{-1} and its energy $\sim 1.5 \times 10^{44}$ erg. These values will be added to those obtained from the model.

For an assumed distance of 3 kpc, we deduce that the mass, scalar momentum and kinetic energy of the ring are respectively $\sim 0.023\,M_\odot$, $\sim 0.6 \times 10^{38}$ gr cm s^{-1} and $\sim 0.04 \times 10^{45}$ erg, where we have assumed that the ring is the region closer to the equatorial plane than 4×10^{16} cm (see Fig. 5). For the rest of the nebula, except for the lobe−tips, we have obtained $\sim 0.056\,M_\odot$, $\sim 3.8 \times 10^{38}$ gr cm s^{-1} and $\sim 0.8 \times 10^{45}$ erg, respectively. (The contribution of the clump seen at ∼−44 km s^{-1} is included.) Finally, the lobe−tips have $M \sim 0.013\,M_\odot$, $P \sim 2.8 \times 10^{38}$ gr cm s^{-1} and $E \sim 1.5 \times 10^{45}$ erg. The total molecular mass of M 2−56 is therefore $\sim 0.092\,M_\odot$, which is very close to that obtained by Bujarrabal et al. (2001).

In Sect. 5.3, we will discuss that the distance of M 2−56 probably is ∼2.1 kpc. In Table 1 a summary of the main distance−dependent nebular parameters is shown for the distances 3 kpc and 2.1 kpc, the last being the kinematic distance. Note that the derived rotational temperatures and column densities, and therefore also the opacities, are distance independent.

It is very interesting to compare the momenta of the different components with the maximum momentum that the stellar radiation, acting on dust grains, can supply (L/c). The ratio $P/(L/c)$, which is distance independent, becomes 1500 yr, 9400 yr and 7000 yr, for the three mentioned regions; the ring, the central part of the nebula without the ring and the lobe−tips. Note that, probably, only the ring has not been accelerated by the post−AGB jets. The stellar radiation needs therefore ∼16 400 yr to supply the observed momentum to the regions accelerated in the post−AGB phase. Since the life of our PPN is < 2400 yr, and the time during which the acceleration took place must be still smaller, the stellar radiation mechanism cannot explain the high momentum carried by the post−AGB ejection. On the other hand, the momentum carried by the central ring can have been supplied by the pressure of the stellar radiation in the AGB phase.

5. The nature of M 2−56

5.1. Comparison with other well studied PPNe

The comparison of the post−AGB lifetimes estimated for M 2−56 (see Sect. 4.1) with those obtained for other nebulae is very interesting, in particular with CRL 618. From PdB observations of CO (unpublished data), the post−AGB outflows of CRL 618 are found to be still inside a slow and spherical molecular envelope, that was probably ejected in the AGB phase, and a kinematical age for the post−AGB flows <100 yr is estimated. The kinematical age of the post−AGB flows of CRL 618 is therefore much smaller than that of the post−AGB flows of M 2−56 (∼1400 yr). We conclude that the envelope of M 2−56 is dynamically more evolved than that of CRL 618. On the other hand, the central stars of both nebulae have been clasified as type B. The lack of photoionized hydrogen in our source (see Trammell et al. 1993), unlike CRL 618, leads to think that the central star of M 2−56 is cooler than that of CRL 618. In conclusion, the nebula of M 2−56 seems much older than that of CRL 618, whereas the central star of M 2−56 probably is slightly less evolved.

Bujarrabal et al. (2001) calculated the kinematical ages of all the PPNe emitting in CO. We have compared the nebular properties of M 2−56 with those PPNe with hotter central stars, obtaining that the molecular envelope of M 2−56 is more evolved in most of the cases. (Note that we have compared M 2−56 with both carbon and oxygen−rich nebulae, since in principle we do not expect that the chemistry plays a role in the evolution of the star, once it has left the AGB, or of the envelope. In fact, we obtain the same conclusions for most sources, independently of their chemistry.)

It is also interesting to compare with the PPN M 1−92. In Bujarrabal et al. (1998b) maps of ^{13}CO emission from M 1−92 are analyzed. From the comparison of the maps of both souces, M 1−92 and M 2−56, and of the position−velocity diagrams, we find that the main difference between them is the lack of emission in an extended part of the lobes of M 2−56. Except for that, the molecular envelopes of both objects are very similar. In addition, also the kinematical age of M 1−92 is smaller than that of M 2−56.

In principle, we could think that the lack of detection of CO emission in part of M 2−56 (in comparison with M 1−92) is due to that this nebula is more evolved, presenting a higher dilution of the gas, which makes the detection of the CO emission very difficult. However, the dilution of the gas probably is not the only responsible for the lack of detection in this extended part. Note that the density distribution (for a constant CO abundance) should present a drastic change at $\sim 2.2 \times 10^{17}$ cm from the equatorial plane, from $\sim 0.4 \times 10^3$ cm^{-3} in the detected region to $< 0.15 \times 10^3$ cm^{-3} in the undetected one (see Sect. 3.2). This sudden decrease of density has not been found for other PPNe, as for example M 1−92 (see Bujarrabal et al. 1998b). That leads us to think that, probably, this lack of detection of the CO emission is mainly consequence of a change in the CO abundance. The densities involved in M 2−56 are so small (unlike M 1−92), that molecular photodissociation produced by interstellar photons can play an important role in the most diluted regions.

We cannot discard that the possible photodissociation be due to UV stellar photons, that could selectively reach the outer regions at high latitudes. However, we think that this explanation is less plausible because there is no detection of a well developed inner photodissociation region (PDR). First, CO is detected in regions very close to the star, probably closer than 10^{16} cm. Second, no fine−structure atomic lines coming from the envelope were detected (data of the ISO archive). Therefore, we propose that the star does not produce enough dissociating photons to significantly destroy CO in the nebula (note that its spectral type is not well known) and/or that they are probably absorbed well before they reach the outer shells, farther than $\sim 10^{17}$ cm from the star, as usually it happens in PPNe (see Castro−Carrizo et al. 2001; Fong et al. 2001). Note that in PPNe and AGB envelopes the PDRs caused by interstellar photons are never detected by ISO.

From the calculations of van Dishoeck & Black (1988) and of Mamon et al. (1988) for the PDRs caused by interstellar photons, we have estimated the CO lifetime expected in different regions of M 2−56, taken into account the thickness of those regions, their densities, and their temperatures. For the region at $\sim 5''$ from the equatorial plane we deduce a CO lifetime of ∼500 yr. That is smaller than the kinematical lifetime estimated for our PPN, ∼2000 yr (for a distance of 3 kpc). Moreover, according to the theoretical models of those authors, the CO abundance decreases drastically from that point where the photodissociation starts being significant. So, taking into account all those factors, we conclude that probably the photodissociation has played an important role in the undetected regions. The lobes would be then complete shells, composed of gas, the detected regions being mostly molecular and the undetected ones being mainly atomic.

On the other hand, as described before, we estimated a CO lifetime of ∼2000 yr for the very center of the nebula, which is similar to the kinematical lifetime estimated for our PPN. The gas in this central part of the nebula remains, therefore, still molecular. However, from those times, we could think that perhaps a significant fraction of the gas in the whole nebula, excepting just the nebular center, is dissociated. We will see later that the total amount of photodissociated gas in M 2−56 may not be very important, but similar to that of other typical PPNe. In any case, note that most of the mass is in the nebular center, where the amount of photodissociated gas is probably negligible.

Finally, for the lobe−tips the predicted CO lifetime is about 800−1000 yr, somewhat smaller than the kinematical lifetime of M 2−56 (see further discussion in Sect. 5.3). This suggests that an important fraction of the gas may be photodissociated in the tips. On the other hand, the appearance of the observed extended clumps at the lobe

tips seems to support the presence of photodissociated gas in the undetected regions. These clumps are extended and irregularly distributed. If CO photodissociation is significant, only the part of the nebula with a column density larger than a certain (photodissociation) limit remains molecular. Then, those clumps would be dense and/or thick enough regions in which photodissociation is not efficient.

5.2. M 2−56; a standard PPN or a low−mass post−AGB object?

An overestimate of the distance could be the origin of those surprising high kinematical times for M 2−56 (in comparison with other nebulae). We remind that the distance of 3 kpc was taken by assuming a typical PPN luminosy of $10^4 L_\odot$. However, note that the molecular mass obtained for that distance ($\sim 0.1\,M_\odot$) is quite low in comparison with other PPNe. We could think that perhaps M 2−56 is not a typical PPN. It may be a low−mass post−AGB object, like 89 Her, M 2−9 and the Red Rectangle (see Bujarrabal et al. 2001). Those objects are characterized by small masses (of the nebula and of the star) and by low luminosities ($\sim 10^3 L_\odot$). If we assume that M 2−56 has the typical luminosity of a low−mass star, $\sim 10^3 L_\odot$, then the distance would be of ∼1 kpc and the molecular mass would be $\sim 0.01\,M_\odot$, similar to that found in the low−mass objects. The kinematical age, for this distance, would be ∼600 yr, comparable to those obtained for other PPNe. However, the discrepancy of the times (for the stars and for the nebulae) observed in CRL 618 and M 2−56 would still hold (see previous section). This discrepancy could be interpreted as a consequence of that the low−mass stars evolve relatively slowly, whereas the nebulae evolve similarly to standard PPNe. (Note that the evolution of the nebula depends on the velocities resulting from the wind interaction, what could be independent of the stellar evolution.) All those points support the idea of that M 2−56 may be a low−mass post−AGB object.

We note, however, that if we compare the CO profiles of M 2−56 with those of other low−mass stars (see Alcolea & Bujarrabal 1991), we find that the high velocity components of M 2−56 reach much higher velocities than those of low−mass objects. Another remarkable difference with the known low−mass objects is in the ratio between the infrared (IR) emission at 60 μm and the integration of the CO(1−0) profile (see Bujarrabal et al. 1992). That ratio for the evolved low−mass objects, as M 2−9 and the Red Rectangle, is more than 10 times higher than that for the standard PPNe, suggesting a large presence of dissociated gas, versus the molecular component, in these low−mass nebulae. The ratio obtained for M 2−56 is similar to those got for typical PPNe, and so smaller than those of low−mass post−AGB stars.

Therefore, though M 2−56 does not seem to be a typical PPN but a low−mass object, in some aspects it shows noticeable differences with the known low−mass nebulae. We conclude that M 2−56 probably is an intermediate object between the known low−mass stars and the typical PPNe. The distance, then, would be between 1 kpc and 3 kpc. (This result is also supported by the discussion in the following section.) A better determination of the distance is however necessary to determine the nature of M 2−56.

5.3. Distance estimate

From the previous discussion we have concluded that the distance of M 2−56 must be between 1 kpc and 3 kpc. In our calculations a distance of 3 kpc has been taken, from the assumption of Goodrich (1991) of a the typical PPN luminosity of $\sim 10^4\,L_\odot$. Goodrich estimated a kinematic distance from a model of the Galactic rotation curve. Due to a wrong assumption on the radial (LSR) velocity (adopted from optical spectroscopy), Goodrich obtained a very large kinematic distance that was ruled out. We will estimate the kinematic distance following the same simple rotation law used by Goodrich, which relates the radial (LSR) velocity, the source position and its distance. A radial (LSR) velocity of -26.1 km s^{-1} (determined precisely in Sect. 3.1) has been substituted, what has led to a kinematic distance of 2.1 kpc. This value supports, therefore, our previous conclusion. See in Table 1 a summary of the main distance−dependent nebular paramenters, for both distances 3 kpc and 2.1 kpc. Note that for those densities obtained for 2.1 kpc, the emission from the nebular center is probably thermalized, being closely thermalized in most of the nebula. The kinetic temperature is probably then very close to the estimated rotational temperature in the whole nebula. The CO lifetime (calculated from van Dishoeck & Black 1988), however, does not change, since it depends only on the column density, which is taken directly from the observations and independently of the distance. So, since the nebular kinematical lifetimes would be ∼1500 yr, our conclusions about the dissociated regions remain (see Sect. 5.1), the photodissociation effects being somewhat less important than for 3 kpc.

The obtained kinematic distance is supported by the statistics perfomed by Pottasch (1984) on the altitudes of PNe (and PPNe) above the Galactic plane. He found that a ∼66% of the nebulae have altitudes smaller than 250 pc. For M 2−56, if we assume a distance of 3 kpc the altitude becomes 440 pc, whereas assuming 2.1 kpc that becomes 300 pc. An assumption for the distance of 2.1 kpc yields a relatively high altitude (∼300 pc) and a relatively low−mass object (the nebula having $\sim 0.05\,M_\odot$), which seems more reasonable. In conclusion, we propose that M 2−56 is placed at ∼2.1 kpc, instead of 3 kpc.

6. Summary

Maps of the emission of ^{12}CO $J = 2{-}1$ and $J = 1{-}0$ from the protoplanetary nebula M 2−56 have been performed using the IRAM interferometer.

As mentioned above, after an extended analysis performed on our data (with other data from the bibliography) of M 2−56, we conclude that the distance probably is ∼2.1 kpc. Here we summarize our main results for 2.1 kpc, the estimated kinematic distance.

Our maps of M 2−56 show a cross−like structure expanding at low velocities and two high−velocity clumps located at 11−15″ from the center along the nebula symmetry axis. This structure, that resembles that seen in other PPNe, allows us to infer the molecular distribution of M 2−56. The CO emission is probably coming from a bipolar nebula, composed of two incomplete contiguous shells that join in the center and expand along the nebula axis. The shells are incomplete because there is no detection of the part of the lobes located from 6″ to 11″, from the nebular center. The intersection of the lobes shapes a dense (approximately edge−on) ring, that expands at ∼7–8 km s^{-1}, and has a typical radius of $\sim 4.2 \times 10^{16}$ cm. This ring is probably the remnant of the AGB circumstellar envelope that has not been accelerated by the interaction with the fast axial post−AGB jets. The nebula axis has an inclination of ∼17° (± 2°) with respect to the plane of the sky, the east−lobe being the closest to us, and its projection on the plane of the sky being very close to the east−west direction (PA ∼ 94°). At the tips of the lobes the gas reaches deprojected expansion velocities of ∼200 km s^{-1} (for $i = 17°$). We obtain a total extent of the nebula of $\sim 9 \times 10^{17}$ cm in the axial direction.

We have developed a nebular model such that the predictions for the CO emission fit satisfactorily the data of both lines. That model allows estimating the physical conditions of the molecular nebula. We have obtained densities from 5×10^3 cm^{-3} in the nebular center to 0.6×10^3 cm^{-3} in the lobe tips, CO rotational temperatures between 13 K and 16 K, and a velocity field composed of a dominant radial component plus an axial contribution. The lobe tips are composed of different clumps, which leads to that the model fitting to those tips is less satisfactory. Opacities in the nebular center of 0.86 and 0.38 have been obtained respectively for the CO $J = 2−1$ and $J = 1−0$ line emission.

From the study of the dynamics we conclude that, the momentum won by the molecular gas in the post−AGB phase is much higher than the maximum momentum that the stellar radiation can carry in a typical PPN life. The radiation pressure mechanism could however explain the linear momentum won in the AGB phase by the central nebular ring. A total mass of the molecular gas of $\sim 0.05\, M_\odot$ has been obtained (for $D = 2.1$ kpc).

The lack of emission observed in an extended part of both lobes, in comparison with other well studied PPNe like, for example, M 1−92, could be due to a noticeable decrease of the CO abundance in the less−dense regions. That may be consequence of the photodissociation of CO, probably caused by interestellar photons in those very tenuous regions. In any case, the total amount of photodissociated gas in M 2−56 does not seem to be very important.

The time elapsed since M 2−56 left the AGB is between 1000 yr and 1700 yr (for $i = 17°$ and $D = 2.1$ kpc), larger than that obtained for other PPNe. Probably M 2−56 is not a typical PPN, but an intermediate object between the known low−mass post−AGB nebulae and the standard PPNe.

Acknowledgements. This work has been financially supported by the Spanish DGES, under project PB96−0104. We acknowledge the IRAM staff from the Plateau de Bure and from Grenoble for carrying the observations and help provided during the data reduction.

References

Alcolea, J., & Bujarrabal, V. 1991, A&A, 245, 499
Alcolea, J., Bujarrabal, V., Sánchez Contreras, C., Neri, R., & Zweigle, J. 2001, A&A, 373, 932
Bujarrabal, V., Alcolea, J., & Planesas, P. 1992, A&A, 257, 701
Bujarrabal, V., Alcolea, J., Neri, R., & Grewing, M. 1997, A&A, 320, 540
Bujarrabal, V., Alcolea, J., Sahai, R., Zamorano, J., & Zijlstra, A. 1998a, A&A, 331, 361
Bujarrabal, V., Alcolea, J., & Neri, R. 1998b, ApJ, 504, 915
Bujarrabal, V., Castro−Carrizo, A., Alcolea, J., & Sánchez Contreras, C. 2001, A&A, 377, 868
Castro−Carrizo, A., Bujarrabal, V., Fong, D., et al. 2001, A&A, 367, 674
Cohen, M., & Kuhi, L. V. 1977, PASP, 89, 829
Fong, D., Meixner, M., Castro−Carrizo, A., et al. 2001, A&A, 367, 652
Goodrich, R. W. 1991, ApJ, 376, 654
Guilloteau, S., Delannoy, J., Downes, D., et al. 1992, A&A, 262, 624
Mamon, G. A., Glassgold, A. E., & Huggins, P. J. 1988, ApJ, 328, 797
Pottasch, S. R. 1984, Astrophys. Space Sci. Libr., 107
Sahai, R., Trauger, J. T., Watson, A. M., et al. 1998, ApJ, 493, 301
Sahai, R., Bujarrabal, V., Castro−Carrizo, A., & Zijlstra, A. 2000, A&A, 360, L9
Trammell, S. R., Dinerstein, H. L., & Goodrich, R. W. 1993, ApJ, 402, 249
Trammell, S. R., & Goodrich, R. W. 1998, AAS, 193, 14.03
van Dishoeck, E. F., & Black, J. H. 1988, ApJ, 334, 771